Evidence for a soft phonon mode driven Peierls-type distortion in Sc_3CoC_4

Jan Langmann [1], Christof Haas [1], Emmanuel Wenger,[2] Dominik Schaniel [2], Wolfgang Scherer,[1] and Georg Eickerling [1,*]

[1]*University of Augsburg, Institut für Physik, Universität Augsburg, Universitätsstraße 1, D-86159 Augsburg, Germany*
[2]*Université de Lorraine, CNRS, CRM2, F-54000 Nancy, France*

We provide experimental and theoretical evidence for the realization of the Peierls-type structurally distorted state in the quasi-one-dimensional superconductor Sc_3CoC_4 by a phonon-softening mechanism. The transition from the high- to the final low-temperature phase below 80 K proceeds via an extended intermediate temperature regime between 80 and 150 K characterized by phonon-driven atom displacements. In support of the low-dimensional character of the title compound we find a highly anisotropic correlation length of these dynamic distortions.

I. INTRODUCTION

Due to recent advances in nanofabrication and nanopatterning dimensionality effects in physical phenomena have become a very active field of research. Even nanowires or two-dimensional films of decidedly three-dimensional materials such as perovskites have become available for further studies [1,2]. Still, the majority of publications in this field is dedicated to a narrow range of materials with structurally inherent low-dimensional features. These are for example $NbSe_3$ [3–6] and $K_{0.3}MoO_3$ [7–10] as representatives of quasi-one-dimensional (quasi-1D) compounds and graphite/graphene [11,12] and transition-metal dichalcogenides [13–18] as representatives of quasi-two-dimensional (quasi-2D) compounds. On the one hand, this focus comes from the weak bonding between their low-dimensional building units easing the fabrication of nanodevices. On the other hand, but even more importantly, intriguing effects of the strongly anisotropic atomic interactions can already be observed in the bulk material.

A characteristic physical phenomenon in many structurally low-dimensional materials is the existence of a subtle competition between a structurally distorted state (e.g., due to the formation of a charge-density wave) and a superconducting state. The balance between these usually conflicting states may be influenced by external factors such as hydrostatic pressure [5,19–22], rapid quenching [18], and chemical pressure via the intercalation or substitution of additional elements [17,23].

The complex carbide Sc_3CoC_4 represents a promising new member in this family of materials: Its structure is coined by quasi-1D infinite $[Co(C_2)_2]$ ribbons orientated along the crystallographic b axis [24–31] and it shows a phase transition into a superconducting state below $T_c = 4.5$ K [27,28,30]. As was recently demonstrated by Wang *et al.*, the superconducting volume fraction of polycrystalline Sc_3CoC_4 samples significantly increases with pressure [32]. At the same time, we have shown in a previous combined x-ray and neutron diffraction study that below approximately 72 K Sc_3CoC_4 undergoes a Peierls-type transition to a low-temperature phase with a doubled translational period along the $[Co(C_2)_2]$ ribbons [27,29,30]. Crystallographically, the transition from the orthorhombic high-temperature (HT) phase (space group *Immm*) to the monoclinic low-temperature (LT) phase (space group $C2/m$) proceeds via a $t2$ followed by an $i2$ transition, leading to a systematic twinning of single crystalline samples in the LT phase [33]. Yet, the driving forces and the exact path to this structurally distorted LT phase remain controversial. In earlier works we interpreted anomalies in the electrical resistivity and the magnetic susceptibility of polycrystalline Sc_3CoC_4 samples as hints to the emergence of a charge-density wave (CDW) below ≈ 140 K [27,29,30]. This interpretation has been challenged by Zhang *et al.* [34]. Their theoretical study provided no evidence of a Fermi surface instability with respect to a CDW of Sc_3CoC_4 in its HT phase. In order to correlate the anomalies in the electrical transport properties with potential structural changes, we performed temperature-dependent x-ray diffraction and resistivity measurements on single-crystalline Sc_3CoC_4 samples.

II. METHODS

Single crystals of Sc_3CoC_4 were grown according to methods described in the literature [26,31,33] and in addition from a lithium metal flux [35]. Needlelike samples with a thickness of ≈ 20 μm and a length of ≈ 200 μm were obtained from the first method and plateletlike samples with a thickness of ≈ 150 μm and a lateral size of ≈ 300 μm from the latter. X-ray diffraction measurements (full details on experiments and employed methods and all data recorded between room temperature and 12 K can be found in the Supplemental Material [36] and Refs. [37–43]) of the temperature-dependent superstructure reflection intensities (10 < T < 160 K) were performed on a HUBER eulerian cradle equipped with a MAR345 image-plate detector and

*georg.eickerling@physik.uni-augsburg.de

operated at the window of a BRUKER FR591 rotating anode (Mo K_α). Additional temperature-dependent single crystal data ($T > 100$ K) were collected on a BRUKER-NONIUS κ goniometer operated at the window of an INCOATEC MicroFocus Tube (Mo K_α). Mapping of diffuse scattering intensities was done employing a HUBER eulerian cradle goniometer equipped with an INCOATEC MicroFocus Tube (Ag K_α) and a PILATUS 300K CdTe detector. Cryogenic temperatures $T > 80$ K were generated by a standard OXFORD open-flow N_2 cooler [44], measurements at $T < 80$ K were performed employing an ARS closed-cycle He cryostat. The handling of parasitic scattering from the vacuum and radiation shields in the closed-cycle cryostat (beryllium domes) was described elsewhere [45]. Numerical values for the intensities of representative superstructure reflections and diffuse features were extracted by image analysis of the collected x-ray diffraction data.

Resistivity measurements of single crystals of Sc_3CoC_4 contacted in a four-point geometry were carried out using a Physical Property Measurement System (PPMS, Quantum Design).

Geometry relaxations of the HT and LT phase of Sc_3CoC_4 starting from the structural parameters from Eickerling *et al.* [30] were performed employing the VASP code [46–49]. The PBE density functional was used throughout [50,51], the energy cutoff for the plane wave basis set was set to 550 eV and a Brillouin grid sampling of $4 \times 4 \times 2$ and $2 \times 2 \times 2$ was used for the HT and LT phase, respectively. Optimizations were stopped when forces were smaller than 0.001 eV/Å.

The PHONOPY code [52] was used for phonon dispersion calculations on Sc_3CoC_4 with a $2 \times 2 \times 2$ supercell. Forces were calculated with the VASP program employing the PBE density functional [50,51], a $4 \times 4 \times 2$ k-point mesh, and an energy cutoff for the plane wave basis set of 500 eV [46–49]. Temperature-dependent thermal diffuse scattering (TDS) simulations were obtained using the *ab2tds* code [53]. The phonon eigenvectors underlying the simulations were generated with PHONOPY on a $24 \times 24 \times 22$ q mesh (containing Γ). In *ab2tds*, the Fourier transform of the dynamical matrix was calculated on a $9 \times 9 \times 9$ mesh of points. Debye-Waller factors for each temperature were computed and reciprocal space planes of TDS intensity were sampled on 100×100 q points for a wavelength of 0.56087 Å and a lower eigenvalue cutoff of 0.001 meV.

III. ELECTRICAL RESISTIVITY

We focus on the results of the electrical resistivity measurements on single crystalline samples of Sc_3CoC_4 first [see Fig. 1(a)]. In accordance with earlier resistivity data from polycrystalline samples [27,30], two anomalies are observed at $T \approx 82$ and 149 K. At both temperatures, the overall metallic decrease of $\rho(T)$ is interrupted by a local increase of the resistivity. The anomaly at 82 K is discerned by a sharp jump in $\rho(T)$ and corresponds to an irreversibility in $\rho(T)$ for polycrystalline samples that permanently displaces the heating against the cooling curve [27,30]. This contrasts with the broader and more gradual character of the anomaly at 149 K.
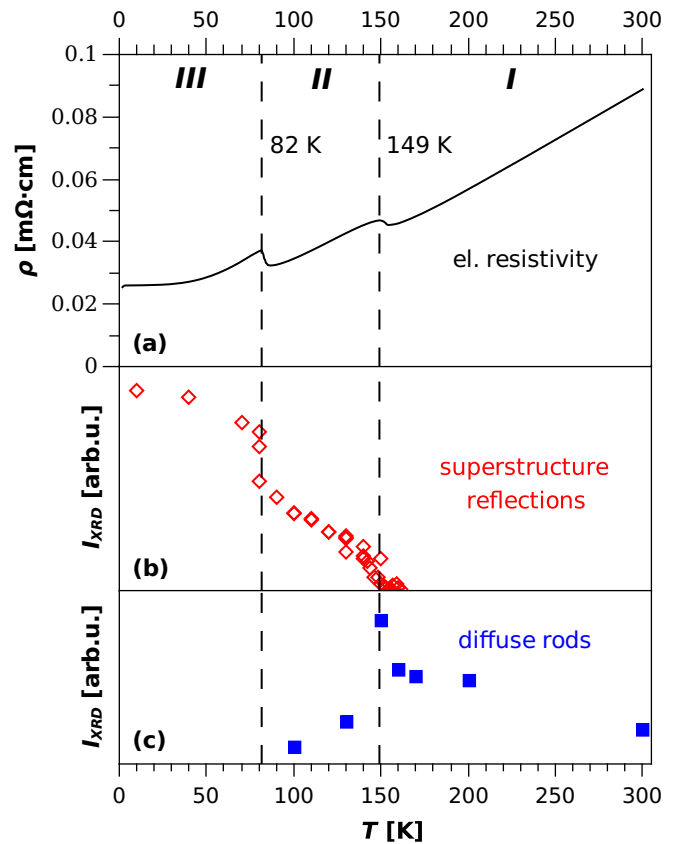
FIG. 1. Temperature dependence of (a) the electrical resistivity $\rho(T)$, (b) the x-ray scattering intensity of superstructure reflections, and (c) the x-ray scattering intensity of diffuse rods $I_{XRD}(T)$ connecting the superstructure reflection positions along c^*.

Details about structural changes connected to the two anomalies in the electrical resistivity are provided by the results of detailed temperature-dependent single-crystal x-ray diffraction measurements on Sc_3CoC_4 outlined in the following.

IV. X-RAY DIFFRACTION

A concise analysis of temperature-dependent changes in diffraction space allows insight into the evolution of the LT structure of Sc_3CoC_4 from the HT structure. The intensity of the superstructure reflections $I_{XRD}(T)$ with $k = (\pm\frac{1}{2}, \pm\frac{1}{2}, 0)$ that result from a fourfold enlargement of the orthorhombic HT unit cell in its *ab* plane [33] represents an appropriate order parameter for the transition from the HT to the LT structure. The simultaneous existence of additional reflections at $k = (+\frac{1}{2}, +\frac{1}{2}, 0)$ and $k = (+\frac{1}{2}, -\frac{1}{2}, 0)$ is due to the systematic twinning caused by the $t2$ transition (a more extensive account of the twinning process in Sc_3CoC_4 and its treatment is available in the Supplemental Material [36] and Refs. [42,54–58]). Note, that all real space and reciprocal space coordinates given hereafter are referred to the orthorhombic HT-phase unit cell.

Our measurements reveal an increase of $I_{XRD}(T)$ [see Fig. 1(b)] in two phenomenologically distinct steps at temperatures between 150 and 80 K (a description of the employed

image analysis techniques for the extraction of $I_{XRD}(T)$ from experimental x-ray diffraction data is provided in the Supplemental Material [36] and Refs. [39–43]). Thereby, $T \approx$ 150 K marks the onset of $I_{XRD}(T)$ followed by a steady increase down to 80 K. At about 80 K, a sharp jump of $I_{XRD}(T)$ is observed. Further cooling towards 10 K entails a saturation of $I_{XRD}(T)$ already below $\approx$ 70 K. We note the close resemblance of this temperature dependence of the superstructure reflection intensity to the observed behavior of $I_{XRD}(T)$ in the charge-density wave material $2H$-TaSe$_2$ [59–61]. In this compound, a sharp step in the superstructure reflection intensities marks a lock-in transition from an incommensurate modulation of the atomic positions at higher temperatures to a commensurate modulation at lower temperatures [59–61]. However, within the available experimental accuracy we could not find hints to the existence of an incommensurate phase in Sc$_3$CoC$_4$, i.e., significant temperature-dependent changes in the superstructure reflection positions or the appearance of higher-order satellite reflections. This puts Sc$_3$CoC$_4$ in a row with the extensively studied transition-metal dichalcogenide $1T$-TiSe$_2$ that shows a Peierls-type structural distortion with a twofold commensurable modulation wave vector k down to a temperature of 8.3 K [15,62–70].

In addition to the pinpoint superstructure reflections strongly temperature-dependent diffuse rods connecting the superstructure reflection positions along c^* can be observed for Sc$_3$CoC$_4$. Representative $(h, 1.5, l)$ reciprocal space planes reconstructed from measuring data at 200 and 12 K and showing exclusively superstructure reflections and diffuse rods are depicted in Figs. 2(a) and 2(b) [36]. Above 200 K, diffuse rod-shaped features without significant intensity modulation along c^* are observed. Upon cooling towards 80 K, a monotonous increase of the intensity at the superstructure reflection positions is paralleled by a lambda-shaped peaking of the diffuse intensity between the superstructure reflection positions at 150 K and its subsequent decay to zero [see Fig. 1(c)] [71]. Below 80 K, only intensity at the superstructure reflection positions remains. This marked temperature dependence along with an anomalous modulation of the diffuse intensity with varying h index [indicated by the profile in the top panel of Fig. 2(a)] rules out crystal defects (e.g., stacking disorder) as the predominant origin of these diffuse features. A detailed discussion of the characteristic variation of the diffuse intensity in reciprocal space can be found in Appendix B.

Moreover, the coinciding positions of both diffuse rods and pinpoint superstructure reflections can be taken as a hint to their common origin. Similar transitions from precursor diffuse features in reciprocal space to pinpoint superstructure reflections are known for other structurally low-dimensional materials featuring low-temperature periodic distortions, e.g., $1T$-TaS$_2$ [13,72], K$_{0.3}$MoO$_3$ [9,73], or NbSe$_3$ [73,74].

Based on the temperature-dependent changes in diffraction space, three different temperature regimes for the structural properties of Sc$_3$CoC$_4$ may be assigned: (I) a HT regime above $\approx$ 150 K characterized by unmodulated (or only weakly) modulated diffuse rods along c^* in reciprocal space, (II) a pre-LT regime between $\approx$ 150 and $\approx$ 80 K with coexistent diffuse rods and weak superstructure reflections,
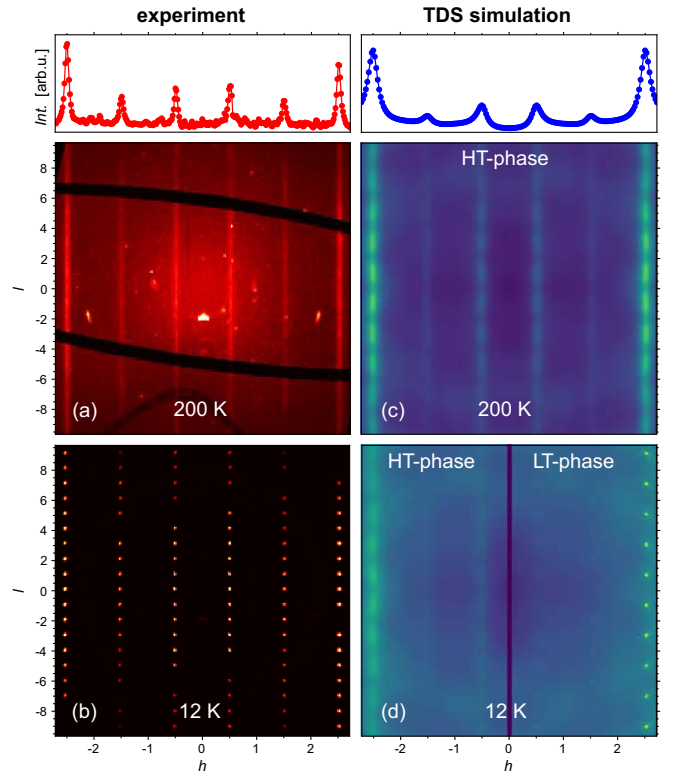
FIG. 2. Comparison of the x-ray scattering features in the $(h, 1.5, l)$ plane of Sc$_3$CoC$_4$ as obtained from experiments at different temperatures [(a) and (b)] and thermal diffuse scattering (TDS) simulations based on *ab initio* calculated phonon dispersion relations for the HT-phase structure [(c) and left part of (d)] and the LT-phase structure of Sc$_3$CoC$_4$ [right part of (d)]. Note that the Miller indices refer to the orthorhombic HT phase and that twinning was not considered in the calculations. 1D profiles of (a) and (c) at $l \approx 2$ are given in the top panel. For details on the simulations, see main text.

and (III) a LT regime below $\approx$ 80 K marked by the exclusive presence of strong and pinpoint superstructure reflections. This partitioning into temperature regimes fits equally well with the anomalies in the electrical resistivity $\rho(T)$ [see Fig. 1(a)]. More specifically, the steady transition between (I) and (II) in $I_{XRD}(T)$ is reflected by a broad uprise in $\rho(T)$ at 149 K. At the same time, the steplike increase of $I_{XRD}(T)$ between (II) and (III) relates to the sharp increase in $\rho(T)$ at 82 K. The differing nature of the transitions at around 80 and 150 K is further emphasized by powder neutron diffraction studies on Sc$_3$CoC$_4$ performed earlier [30]. Therein, steplike lattice parameter changes with sudden increases in b and c and a decrease in a were observed upon cooling of the samples to below 80 K. There was no evidence for a comparable anomaly in a, b, and c in the temperature region around 150 K.

V. DISCUSSION

Starting point for the interpretation of the above results is the structural model of the Sc$_3$CoC$_4$ HT phase. The existence of rod-shaped features in diffraction space may be related to layered structural moieties in real space. Taking into account the orientation of the rods along c^*, these layers must extend
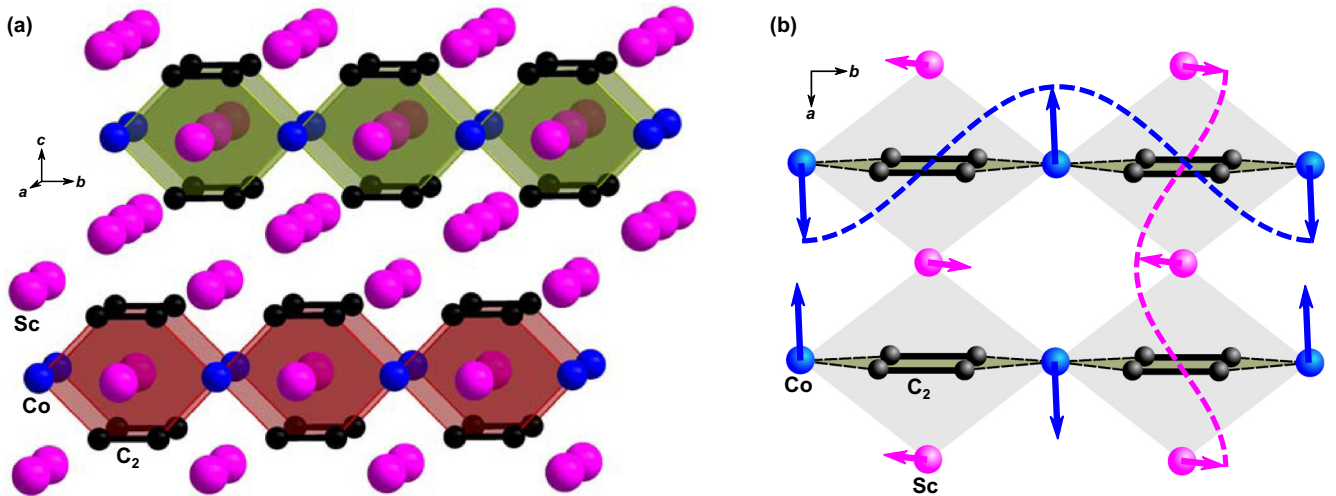
FIG. 3. Ball-and-stick representation of the layered building units of HT Sc₃CoC₄ in (a) the crystallographic *bc* plane and (b) the crystallographic *ab* plane of the orthorhombic unit cell. In (b) the sinusoidal displacive modulation of the cobalt and scandium atom positions as observed for the low-frequency phonon modes between *W* and *T* (see text) and the monoclinic LT phase [30] is indicated by arrows.

parallel to the crystallographic *ab* plane of the orthorhombic HT cell and can be associated with stacked ribbons of interconnected [Co(C₂)₂Co] hexagons [shaded in red and green in Fig. 3(a)].

In a simplistic picture, the diffuse rods may be attributed to disorder between the layered building units of the HT structure along *c*. However, the characteristic intensity modulation of the rod intensity perpendicular to *c** [see profile above Fig. 2(a)] precludes an explanation in terms of a static stacking disorder involving the slippage of complete layers (see Appendix B). An alternative explanation for the occurrence of diffuse intensity above 80 K might be provided by precursor dynamic fluctuations along the displacement coordinates of the static Peierls-type distortion evolving below 80 K. The temperature-dependent contraction of the diffuse intensity into superstructure reflections between 150 and 80 K may in turn be linked to the softening of a phonon mode at $k = (\frac{1}{2}, \frac{1}{2}, 0)$ [30].

In Fig. 4 the phonon dispersion of Sc₃CoC₄ is shown along selected lines of the first Brillouin zone (BZ) of the orthorhombic HT phase. Along the path W $(\frac{1}{2}, \frac{1}{2}, \frac{1}{2})$-$T$ $(\frac{1}{2}, \frac{1}{2}, 0)$ a low-frequency branch with marginal dispersion can be identified. The displacement pattern corresponding to the mode at *T* is in close analogy to the static displacement pattern in the LT phase of Sc₃CoC₄ [30]. Furthermore, the path *W*-*T* of the low-lying phonon branch can be correlated with the course of the diffuse rods in reciprocal space (see Appendix A) [75,76]. Figuratively, its flat course can be interpreted in terms of equal excitation energies for an infinite set of dynamic LT-phaselike displacements of the cobalt and scandium atoms [illustrated in Fig. 3(b) for a layer section in the *ab* plane] with differing modulations along the stacking direction *c* [71]. The superposition of all these dynamic displacements yields the picture of disorder between the layered building units of Sc₃CoC₄. In fact, a similar behavior connected to weak coupling between layered building units has been observed for other compounds such as the francisite Cu₃Bi(SeO₃)₂O₂Cl. In the phonon dispersion of its HT phase, a nearly dispersionless

branch connects a zone-center mode at Γ with equal atom displacements in all constituting layers to a modulated variant of the mode at Z with layer-wise inverted atom displacements [77].

To underline the correspondence between diffuse rods in x-ray diffraction and a soft branch in the phonon dispersion we performed simulations of the thermal diffuse scattering (TDS) contribution to the diffracted intensity in the $(h, 1.5, l)$ plane. Consistent with the inferences made above, simulations based on the phonon dispersion of the HT phase of Sc₃CoC₄ and assuming a temperature of 200 K (Fig. 4) reproduce the experimental observations not only in the general positions and direction of the rods, but even in details like the nontrivial intensity variations along the a^* direction. A comparison between the experimentally obtained $(h, 1.5, l)$ plane at 200 K and the TDS simulation for the HT phase of Sc₃CoC₄ is given in Figs. 2(a) and 2(c) with corresponding profiles in the top
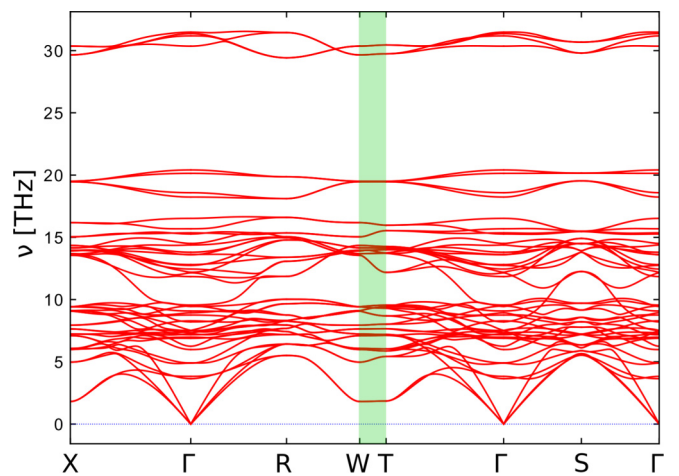
FIG. 4. Calculated phonon dispersion along selected high-symmetry paths in the Brillouin zone of HT Sc₃CoC₄. The path between W $(\frac{1}{2}, \frac{1}{2}, \frac{1}{2})$ and T $(\frac{1}{2}, \frac{1}{2}, 0)$ is highlighted.

panel. The weak modulation of the simulated TDS intensity with a period of two reciprocal lattice constants along c^* in Fig. 2(c) is most likely due to numerical artifacts introduced by a Fourier interpolation step and not supported by reciprocal space reconstructions based on x-ray diffraction data. Key properties of the phonon dispersion remain unaffected by this problem as is demonstrated in the Supplemental Material [36] (see also Refs. [53,78]).

The phonon dispersion of the HT phase of Sc_3CoC_4, however, cannot explain the gradual vanishing of the diffuse rods between 150 and 80 K and the appearance of pinpoint superstructure reflections. Figure 2(b) shows a reconstruction of the $(h, 1.5, l)$ plane from measuring data at 12 K illustrating the extensive reorganization of the x-ray diffraction pattern below 80 K. To account for these changes, a phonon softening mechanism may be invoked that selectively reduces the frequency of the phonon mode at T in the soft W-T branch to zero. Simultaneously with the increasing dispersion between W and T comes a preference for LT-phaselike dynamic atom displacements without superimposed modulation along c and a progressive structural ordering. Zero phonon frequency at T is reached at 80 K resulting in the formation of the LT phase of Sc_3CoC_4 with static atom displacements from the equilibrium positions in the HT phase. Consequently, no more prominent diffuse features are found in TDS simulations of the $(h, 1.5, l)$ plane at 12 K employing the phonon eigenvalues of the LT phase [30] [see right part of Fig. 2(d)] (a plot of the phonon dispersion for the LT-phase structure of Sc_3CoC_4 can be found in the Supplemental Material [36]). Only localized TDS contributions at positions of the experimentally observed superstructure reflections remain, consistent with a doubling of the unit cell. We note that twinning was not considered within the simulations and thus each second reflection position is missing in Fig. 2(d). That the rearrangement of diffuse features in reciprocal space cannot be attributed to temperature effects alone is illustrated by TDS simulations for the HT-phase structure of Sc_3CoC_4 at 12 K [left part of Fig. 2(d)]. Without a structural transition weak diffuse rods would still be present at this temperature. Again, parallels to the francisite $Cu_3Bi(SeO_3)_2O_2Cl$ may be drawn, where cooling induces a successive frequency reduction of the phonon mode at Z in the soft Γ-Z branch setting the stage to a displacive transition into a static LT phase with doubled c parameter at 115 K [77,79].

We may thus propose a consistent model for the observations in electrical resistivity and intensity-weighted reciprocal space: In the HT regime [(I), see Fig. 1] above 150 K, dynamic disorder driven by the phonon modes W-T leads to the occurrence of diffuse rods in reciprocal space. At approximately 150 K, the mode at T starts to soften, thus continuously reducing the degree of thermal fluctuations in the pre-LT regime (II) and leading to the successive ordering of the layers stacked in c direction. Around 80 K, the softening process is complete and the displacement pattern of the phonon mode freezes into the static atomic positions observed in the LT phase (III) of Sc_3CoC_4.

VI. CONCLUSION

To conclude, we provide experimental and theoretical evidence for a soft-phonon-driven formation of a Peierls-type structurally distorted state in Sc_3CoC_4 upon cooling. Based on the new results, the interplay between two distinct transitions, i.e., a charge-density wave transition at 150 K and a Peierls-type distortion at 80 K, discussed in earlier publications [27,29,30,34], can now be consistently described by a single extended structural phase transition via an intermediate state between 80 and 150 K. This intermediate state is characterized by phonon-driven dynamic atom displacements in the crystallographic *ab* plane with strongly temperature-dependent frequency and correlation length along the *c* axis. Inelastic x-ray or neutron scattering experiments might provide further information on the progression of the phonon-softening mechanism towards the static structurally distorted LT phase observed below 80 K.

APPENDIX A: INTERPRETATION OF DIFFUSE X-RAY SCATTERING INTENSITY: RELATION TO THE PHONON DISPERSION

In the following we outline the theoretical background for the interpretation of the diffuse rods observed in reciprocal space for Sc_3CoC_4 in temperature regimes (I) and (II) (above ≈ 80 K) in terms of thermal diffuse scattering (TDS).

We focus on the first-order TDS intensity given by the sum over the absolute squares of the dynamical structure factor contributions F_j for all phonons j:

$$I_1(\mathbf{q}) = \frac{\hbar N I_e}{2} \sum_j \frac{1}{\omega_{\mathbf{q},j}} \coth\left(\frac{\hbar \omega_{\mathbf{q},j}}{2 k_B T}\right) |F_j(\mathbf{q})|^2, \qquad (A1)$$

where the number of unit cells is denoted by N and the one-electron scattering intensity by I_e. Every sum contribution is weighted by a thermal occupation factor $\frac{1}{\omega_{\mathbf{q},j}} \coth\left(\frac{\hbar \omega_{\mathbf{q},j}}{2 k_B T}\right)$ for phonon j at wave vector $\mathbf{q}$ with frequency $\omega_{\mathbf{q},j}$ [76]. Thus, the contributions of low-frequency phonons to TDS are dominant. The dynamical structure factors F_j derive from the phonon-specific shift of the atoms s in the unit cell as

$$F_j(\mathbf{q}) = \sum_s \frac{f_s}{\sqrt{\mu_s}} \exp(-M_s)(\mathbf{q} \cdot \mathbf{e}_{\mathbf{q},j,s}), \qquad (A2)$$

with atomic scattering factor f_s, atomic mass μ_s, and Debye-Waller factor M_s. Size and direction of the atom shifts are described by the polarization vector $\mathbf{e}_{\mathbf{q},j,s}$ [76]. Special attention should be paid to the double meaning of the wave vector $\mathbf{q}$: On the one hand, $\mathbf{q}$ is the sum of the reduced phonon wave vector in the first Brillouin zone $\mathbf{k}$ and a reciprocal lattice vector $\mathbf{K_q}$,

$$\mathbf{q} = \mathbf{k} + \mathbf{K_q}. \qquad (A3)$$

Due to the periodicity of the phonon dispersion in reciprocal space, $\omega_{\mathbf{q},j}$ and $\omega_{\mathbf{k},j}$ are identical. On the other hand, $\mathbf{q}$ indicates the position of the considered TDS feature and $\mathbf{K_q}$ the position of the adjacent Bragg reflection in reciprocal space.

The dominant diffuse reciprocal space features in the HT regime of Sc_3CoC_4 are the rods along c^*. The location of all points on the diffuse rods with respect to the adjacent Bragg reflections can be described by wave vectors $\mathbf{k} = (\frac{1}{2}, \frac{1}{2}, l)$ with l varying between 0 and $\frac{1}{2}$. Thereby the boundary points
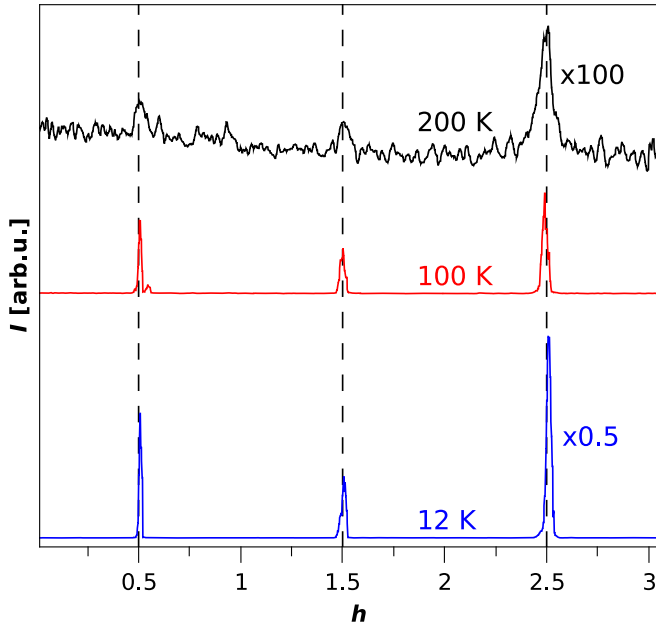
FIG. 5. Intensity profiles along $[h, 1.5, 0]$ at 200 K (HT regime), at 100 K (pre-LT regime), and at 12 K (LT regime). All reflection indices refer to the orthorhombic HT-phase unit cell of Sc_3CoC_4. For clarity, the profiles at 200 and 12 K were scaled by factors of 100 and 0.5, respectively. In all cases, an alternation between strong and weak intensity along h becomes evident.

$\mathbf{k} = (\frac{1}{2}, \frac{1}{2}, 0)$ and $\mathbf{k} = (\frac{1}{2}, \frac{1}{2}, \frac{1}{2})$ represent positions on and exactly midway between the superstructure reflections appearing in the pre-LT and LT regime. From this information, a low-frequency, flat phonon branch connecting the zone boundaries at W ($\hateq \frac{1}{2}, \frac{1}{2}, \frac{1}{2}$) and T ($\hateq \frac{1}{2}, \frac{1}{2}, 0$) may be postulated for the HT regime. Indeed, an acoustic phonon mode with extraordinarily low frequency between W and T is found in the *ab initio* phonon dispersion relation based on the idealized ground-state structure of HT Sc_3CoC_4 (highlighted in green in Fig. 4).

APPENDIX B: INTERPRETATION OF DIFFUSE X-RAY SCATTERING INTENSITY: INTENSITY MODULATIONS

Focusing on the intensity modulation of the TDS, diffuse rods and pinpoint superstructure reflections show similar intensity alternations along the reciprocal space directions a^* and b^* (see Fig. 2). More specifically, rows of weaker superstructure reflections or diffuse rods along c^* are invariably followed by rows of stronger superstructure reflections or diffuse rods and vice versa. Thereby the intensity of both weak and strong reciprocal space features rises with increasing h or k index. In Fig. 5, representative line profiles of the scattering intensity along $[h, 1.5, 0]$ cutting through the superstructure reflection positions in the $(h, 1.5, l)$ plane are shown for each of the temperature regimes of Sc_3CoC_4 postulated in Sec. V. The similarity of the line profiles in Fig. 5 may be taken as a hint to (i) the common origin of diffuse rods and pinpoint superstructure reflections and (ii) a persistent displacive modulation of the atom positions in the *ab* plane with

temperature-dependent correlation length along c as opposed to simple stacking disorder.

In the following we will relate the characteristic scattering intensity variation along the line $[h, 1.5, 0]$ to a simplified model of the displacive modulation pattern in Sc_3CoC_4. Only scattering contributions from the set of atoms most affected by shifts from their high-symmetry positions, i.e., the cobalt and the scandium atoms capping the $[Co(C_2)_2Co]$ hexagons (see Fig. 3), are taken into account. The effect of the shifts in the carbon atom positions is neglected due to the relatively small scattering cross section of carbon compared to scandium and cobalt. Furthermore, only the scattering contributions from one of two twin domains are considered (*vide supra*). The contributions of the second domain may be symmetry generated by application of the according twin law.

In a first step, the contributions of the cobalt and scandium atoms to the structure factor $F(\mathbf{h})$ are treated separately. The general structure factor equation for a one-atom structure subjected to an arbitrary displacement wave is detailed elsewhere [80,81]. Assuming a perfectly commensurate modulation the structure factor of Sc_3CoC_4 at the position of superstructure reflections can be described by the simplified formula

$$F(\mathbf{h}) = J_1(2\pi \mathbf{h}\mathbf{a}) \exp(i\phi) G(\mathbf{h} + \mathbf{q})$$
$$- J_1(2\pi \mathbf{h}\mathbf{a}) \exp(-i\phi) G(\mathbf{h} - \mathbf{q}). \quad (B1)$$

The position of the superstructure reflections is referred to by the reciprocal space vector $\mathbf{h}$, while $G(\mathbf{h})$ and $J_1(2\pi \mathbf{h}\mathbf{a})$ denote the structure factor of the unmodulated structure and the first-order Bessel function, respectively. The displacement wave is characterized by its amplitude vector $\mathbf{a}$, wave vector $\mathbf{q}$, and phase ϕ.

Concerning the cobalt substructure, a phase $\phi = 0$ may be put for the displacements [82] leading to

$$F_{Co}(\mathbf{h}) = J_1(2\pi \mathbf{h}\mathbf{a}) \cdot G_{Co}(\mathbf{h} + \mathbf{q})$$
$$- J_1(2\pi \mathbf{h}\mathbf{a}) \cdot G_{Co}(\mathbf{h} - \mathbf{q}), \quad (B2)$$

so that in a first step the variation of $J_1(2\pi \mathbf{h}\mathbf{a})$ and $G(\mathbf{h})$ along the line $[h, 1.5, 0]$ must be considered. As the cobalt atom displacements are directed along the crystallographic a direction $[\mathbf{a} = (a, 0, 0)^T]$, the argument of J_1 reduces to the scalar ha. Nonzero values of $G_{Co}(\mathbf{h} \pm \mathbf{q})$ may only occur, if a vector $\pm\mathbf{q} = \pm(0.5, 0.5, 0)^T$ connects the reciprocal space position $\mathbf{h}$ of the considered superstructure reflection to the position of a nonextinct main reflection [83]. In accord with the two possible signs of $\mathbf{q}$, there are always two contributing main reflection positions in the $(h, k, 0)$ plane for each superstructure reflection (see Fig. 6).

However, every second superstructure reflection along $[h, 1.5, 0]$ is absent (crossed out in Fig. 6), because its associated main reflections are extinct due to the body centering of the HT Sc_3CoC_4 crystal structure. Due to the small variation of the atomic scattering factors over the narrow considered range of h values, the structure factors $G_{Co}(\mathbf{h} \pm \mathbf{q})$ for the contributing main reflections of the unmodulated Co substructure [84] depend only weakly on h with $G_{Co}(\mathbf{h} + \mathbf{q}) > 0$ and $G_{Co}(\mathbf{h} - \mathbf{q}) \approx -G_{Co}(\mathbf{h} + \mathbf{q})$. Thus, the variation of the superstructure reflection structure factor $F_{Co}(\mathbf{h})$ along $[h, 1.5, 0]$
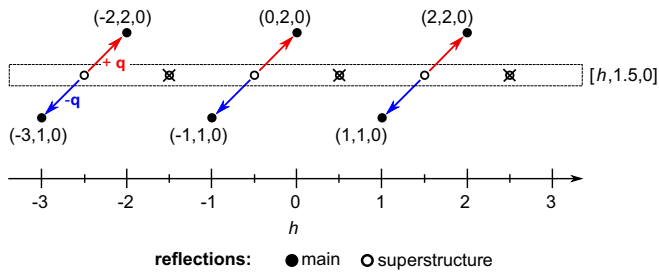
FIG. 6. Position of the main reflections in the $(h, k, 0)$ plane contributing to the structure factor of the superstructure reflections along the line $[h, 1.5, 0]$. All reflection indices are referred to the orthorhombic HT-phase unit cell of Sc_3CoC_4. The wave vectors $+\mathbf{q}$ and $-\mathbf{q}$ connecting the superstructure reflections to the main reflections are displayed in red and blue, respectively. Absent superstructure reflections are crossed out (see text).

in good approximation mirrors the behavior of the Bessel function $J_1(2\pi ha)$ [see solid blue line in Fig. 7(a)].

The same strategy can be applied in the derivation of the structure factor contribution of the scandium atoms $F_{Sc}(\mathbf{h})$. Displacements of the scandium atoms towards long $Co\cdots Co$ contacts [85] are accounted for by putting a value of π for the displacement wave phase ϕ, so that

$$F_{Sc}(\mathbf{h}) = -J_1(2\pi \mathbf{h}a) \cdot G_{Sc}(\mathbf{h} + \mathbf{q})$$
$$+ J_1(2\pi \mathbf{h}a) \cdot G_{Sc}(\mathbf{h} - \mathbf{q}) \quad (B3)$$

is obtained. In contrast to the cobalt atoms, the scandium atom displacements point along the crystallographic b direction $[\mathbf{a} = (0, a, 0)^T]$, so that the argument $\mathbf{h}a$ of the Bessel functions in Eq. (B3) is constant along $[h, 1.5, 0]$ and $J_1(\mathbf{h}a) =$ const. > 0 over the whole range of h values. Approximating the structure factor for the contributing main reflections of the unmodulated scandium substructure [86] in analogy to the cobalt atom substructure again yields a weakly h-dependent value of $G_{Sc}(\mathbf{h} \pm \mathbf{q})$ with $G_{Sc}(\mathbf{h} + \mathbf{q}) > 0$ and $G_{Sc}(\mathbf{h} - \mathbf{q}) \approx -G_{Sc}(\mathbf{h} + \mathbf{q})$. Therefore, the structure factor contribution $F_{Sc}(\mathbf{h})$ of the Sc atoms at the superstructure reflection positions along $[h, 1.5, 0]$ shows only slight variation with h and is invariably negative [see solid orange line in Fig. 7(a)]. Finally, the structure factor contributions $F_{Co}(\mathbf{h})$ and $F_{Sc}(\mathbf{h})$ of cobalt
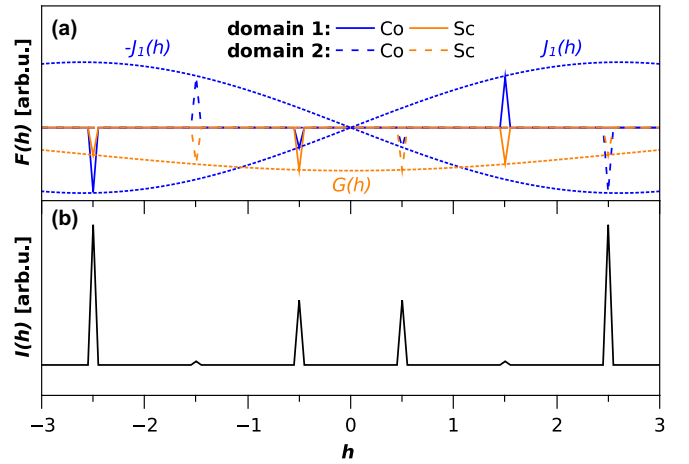
FIG. 7. Simulation [88] of the contributions to $F(\mathbf{h})$ along $[h, 1.5, 0]$ (referring to the orthorhombic HT-phase unit cell of Sc_3CoC_4) for a simplified modulated Sc_3CoC_4 structure: (a) cobalt atom contributions are given in blue with tentative enveloping first-order Bessel functions $J_1(h)$ and $-J_1(h)$. Scandium atom contributions are given in orange with an enveloping Gaussian function $G(h)$ as approximation for the angle dependence of the atomic scattering factor of scandium. Scattering due to domain 1 is signified by solid lines, scattering due to domain 2 by hatched lines. The summed up and squared structure factor contributions (b) reproduce the experimentally observed intensity alternation scheme along $[h, 1.5, 0]$.

and scandium along $[h, 1.5, 0]$ can be summed up and also the structure factor contributions of the second Sc_3CoC_4 domain can be generated at this stage by mirroring the contributions from the first domain at the y axis [87] [hatched lines in Fig. 7(a)]. At every second superstructure reflection position (counted from $h = 0$) opposite signs of $F_{Sc}(\mathbf{h})$ and $F_{Co}(\mathbf{h})$ meet to yield a small absolute value of the total structure factor $F(\mathbf{h})$. In contrast, at superstructure reflection positions with uneven number equal signs of $F_{Sc}(\mathbf{h})$ and $F_{Co}(\mathbf{h})$ meet to yield a large absolute value of $F(\mathbf{h})$. Taking the absolute square of the summed structure factor profile leads to the observed characteristic intensity modulation for diffuse rods and pinpoint superstructure reflections along $[h, 1.5, 0]$ in Sc_3CoC_4 [see Fig. 7(b)].

[1] A. P. Schlaus, M. S. Spencer, K. Miyata, F. Liu, X. Wang, I. Datta, M. Lipson, A. Pan, and X.-Y. Zhu, Nat. Commun. **10**, 265 (2019).

[2] D. Ji, S. Cai, T. R. Paudel, H. Sun, C. Zhang, L. Han, Y. Wei, Y. Zang, M. Gu, Y. Zhang, W. Gao, H. Huyan, W. Guo, D. Wu, Z. Gu, E. Y. Tsymbal, P. Wang, Y. Nie, and X. Pan, Nature (London) **570**, 87 (2019).

[3] A. Meerschaut and J. Rouxel, J. Less-Common Met. **39**, 197 (1975).

[4] J. L. Hodeau, M. Marezio, C. Roucau, R. Ayroles, A. Meerschaut, J. Rouxel, and P. Monceau, J. Phys. C: Solid State Phys. **11**, 4117 (1978).

[5] M. N. Regueiro, J.-M. Mignot, and D. Castello, Europhys. Lett. **18**, 53 (1992).

[6] L. Yang, Y. Tao, J. Liu, C. Liu, Q. Zhang, M. Akter, Y. Zhao, T. T. Xu, Y. Xu, Z. Mao, Y. Chen, and D. Li, Nano Lett. **19**, 415 (2019).

[7] J. Graham and A. D. Wadsley, Acta Crystallogr. **20**, 93 (1966).

[8] G. Travaglini, P. Wachter, J. Marcus, and C. Schlenker, Solid State Commun. **37**, 599 (1981).

[9] J. P. Pouget, S. Kagoshima, C. Schlenker, and J. Marcus, J. Phys. Lett. **44**, 113 (1983).

[10] K. Inagaki and S. Tanda, Phys. Rev. B **97**, 115432 (2018).

[11] K. S. Novoselov, A. K. Geim, S. V. Morozov, D. Jiang, Y. Zhang, S. V. Dubonos, I. V. Grigorieva, and A. A. Firsov, Science **306**, 666 (2004).

[12] Y. Cao, V. Fatemi, S. Fang, K. Watanabe, T. Taniguchi, E. Kaxiras, and P. Jarillo-Herrero, Nature (London) **556**, 43 (2018).

[13] P. M. Williams, G. S. Parry, and C. B. Scrub, Philos. Mag. **29**, 695 (1974).

[14] S.-H. Lee, J. S. Goh, and D. Cho, Phys. Rev. Lett. **122**, 106404 (2019).

[15] H. P. Hughes, J. Phys. C: Solid State Phys. **10**, L319 (1977).

[16] G.-J. Shu, Y. Zhou, M.-Y. Kao, C. J. Klingshirn, M. R. S. Huang, Y.-L. Huang, Y. Liang, W. C. H. Kuo, and S.-C. Liou, Appl. Phys. Lett. **114**, 202103 (2019).

[17] S. Pyon, K. Kudo, and M. Nohara, J. Phys. Soc. Jpn. **81**, 053701 (2012).

[18] H. Oike, M. Kamitani, Y. Tokura, and F. Kagawa, Sci. Adv. **4**, eaau3489 (2018).

[19] M. Ido, Y. Okayama, T. Ijiri, and Y. Okajima, J. Phys. Soc. Jpn. **59**, 1341 (1990).

[20] S. Yasuzuka, K. Murata, T. Fujimoto, M. Shimotori, and K. Yamaya, J. Phys. Soc. Jpn. **74**, 1782 (2005).

[21] P. Monceau, Adv. Phys. **61**, 325 (2012).

[22] A. Kiswandhi, J. S. Brooks, H. B. Cao, J. Q. Yan, D. Mandrus, Z. Jiang, and H. D. Zhou, Phys. Rev. B **87**, 121107(R) (2013).

[23] J. J. Yang, Y. J. Choi, Y. S. Oh, A. Hogan, Y. Horibe, K. Kim, B. I. Min, and S.-W. Cheong, Phys. Rev. Lett. **108**, 116402 (2012).

[24] W. Jeitschko, M. H. Gerss, R.-D. Hoffmann, and S. Lee, J. Less-Common Met. **156**, 397 (1989).

[25] A. Tsokol', O. I. Bodak, and E. P. Marusin, Sov. Phys. Crystallogr. **31**, 466 (1986).

[26] B. Rohrmoser, G. Eickerling, M. Presnitz, W. Scherer, V. Eyert, R.-D. Hoffmann, U. C. Rodewald, C. Vogt, and R. Pöttgen, J. Am. Chem. Soc. **129**, 9356 (2007).

[27] W. Scherer, C. Hauf, M. Presnitz, E.-W. Scheidt, G. Eickerling, V. Eyert, R.-D. Hoffmann, U. C. Rodewald, A. Hammerschmidt, C. Vogt, and R. Pöttgen, Angew. Chem., Int. Ed. **49**, 1578 (2010).

[28] E.-W. Scheidt, C. Hauf, F. Reiner, G. Eickerling, and W. Scherer, J. Phys.: Conf. Ser. **273**, 012083 (2011).

[29] W. Scherer, G. Eickerling, C. Hauf, M. Presnitz, E.-W. Scheidt, V. Eyert, and R. Pöttgen, *Modern Charge-Density Analysis*, 1st ed., edited by C. Gatti and P. Macchi (Springer, Netherlands, 2012), Chap. 10, pp. 359–385.

[30] G. Eickerling, C. Hauf, E.-W. Scheidt, L. Reichardt, C. Schneider, A. Muñoz, S. Lopez-Moreno, A. H. Romero, F. Porcher, G. André, R. Pöttgen, and W. Scherer, Z. Anorg. Allg. Chem. **639**, 1985 (2013).

[31] M. He, C. H. Wong, D. Shi, P. L. Tse, E.-W. Scheidt, G. Eickerling, W. Scherer, P. Sheng, and R. Lortz, J. Phys.: Condens. Matter **27**, 075702 (2015).

[32] E. Wang, X. Zhu, and H.-W. Wen, Europhys. Lett. **115**, 27007 (2016).

[33] C. Vogt, R.-D. Hoffmann, U. C. Rodewald, G. Eickerling, M. Presnitz, V. Eyert, W. Scherer, and R. Pöttgen, Inorg. Chem. **48**, 6436 (2009).

[34] C. Zhang, J. S. Tse, K. Tanaka, and H.-Q. Lin, Europhys. Lett. **100**, 67003 (2012).

[35] C. D. Haas, Ph.D. thesis, University of Augsburg, 2019.

[36] See Supplemental Material at http://link.aps.org/supplemental/10.1103/PhysRevB.102.094109 for information on investigated samples, experimental techniques and TDS simulations as well as a full set of temperature-dependent reciprocal-space maps.

[37] M. Natarajan, A. Das, and C. Rao, Trans. Faraday Soc. **65**, 3081 (1969).

[38] E. Wenger, S. Dahaoui, P. Alle, P. Parois, C. Palin, C. Lecomte, and D. Schaniel, Acta Crystallogr. Sect. B **70**, 783 (2014).

[39] J. Langmann, A. Fischer, and G. Eickerling, *htd2predict* (University of Augsburg, Augsburg, Germany, 2019).

[40] M. A. Estermann and W. Steurer, Phase Transit. **67**, 165 (1998).

[41] A. J. M. Duisenberg, J. Appl. Crystallogr. **25**, 92 (1992).

[42] A. J. M. Duisenberg, L. M. J. Kroon-Batenburg, and A. M. M. Schreurs, J. Appl. Crystallogr. **36**, 220 (2003).

[43] C. A. Schneider, W. S. Rasband, and K. W. Eliceiri, Nat. Methods **9**, 671 (2012).

[44] J. Cosier and A. M. Glazer, J. Appl. Crystallogr. **19**, 105 (1986).

[45] A. Reisinger, N. Trapp, I. Krossing, S. Altmannshofer, V. Herz, M. Presnitz, and W. Scherer, Angew. Chem., Int. Ed. **46**, 8295 (2007).

[46] G. Kresse and J. Furthmüller, Comput. Mater. Sci. **6**, 15 (1996).

[47] G. Kresse and J. Furthmüller, Phys. Rev. B **54**, 11169 (1996).

[48] G. Kresse and J. Hafner, Phys. Rev. B **49**, 14251 (1994).

[49] G. Kresse and J. Hafner, Phys. Rev. B **47**, 558 (1993).

[50] J. P. Perdew, K. Burke, and M. Ernzerhof, Phys. Rev. Lett. **77**, 3865 (1996).

[51] J. P. Perdew, K. Burke, and M. Ernzerhof, Phys. Rev. Lett. **78**, 1396 (1997).

[52] A. Togo and I. Tanaka, Scr. Mater. **108**, 1 (2015).

[53] B. Wehinger and A. Mirone, ab2tds, ESRF—The European Synchrotron (2013), http://ftp.esrf.fr/scisoft/AB2TDS/.

[54] T. Hahn and H. Klapper, *International Tables for Crystallography*, 2nd ed. (John Wiley & Sons, New York, 2014), Vol. D, Chap. 3.3, pp. 413–483.

[55] L. Krause, R. Herbst-Irmer, G. M. Sheldrick, and D. Stalke, J. Appl. Crystallogr. **48**, 3 (2015).

[56] G. M. Sheldrick, ACA RefleXions **3**, 41 (2015).

[57] G. M. Sheldrick (unpublished).

[58] Incoatec GmbH, IμS for Ag-K$_\alpha$ Radiation (2015).

[59] D. E. Moncton, J. D. Axe, and F. J. DiSalvo, Phys. Rev. Lett. **34**, 734 (1975).

[60] D. E. Moncton, J. D. Axe, and F. J. DiSalvo, Phys. Rev. B **16**, 801 (1977).

[61] P. M. Williams, *Crystallography and Crystal Chemistry of Materials with Layered Structures*, 1st ed., edited by F. Lévy, Physics and Chemistry of Materials with a Layered Structure (Springer Netherlands, 1976), Vol. 2, Chap. 2, pp. 51–92.

[62] C. S. Snow, J. F. Karpus, S. L. Cooper, T. E. Kidd, and T.-C. Chiang, Phys. Rev. Lett. **91**, 136402 (2003).

[63] A. F. Kusmartseva, B. Sipos, H. Berger, L. Forro, and E. Tutiš, Phys. Rev. Lett. **103**, 236401 (2009).

[64] S. Sugai, K. Murase, S. Uchida, and S. Tanaka, Solid State Commun. **35**, 433 (1980).

[65] N. Wakabayashi, H. Smith, K. Woo, and F. Brown, Solid State Commun. **28**, 923 (1978).

[66] M. Holt, P. Zschack, H. Hong, M. Y. Chou, and T.-C. Chiang, Phys. Rev. Lett. **86**, 3799 (2001).

[67] F. J. Di Salvo, D. E. Moncton, and J. V. Waszczak, Phys. Rev. B **14**, 4321 (1976).

[68] F. C. Brown, Physica B+C **99**, 264 (1980).

[69] T. E. Kidd, T. Miller, M. Y. Chou, and T.-C. Chiang, Phys. Rev. Lett. **88**, 226402 (2002).

[70] Y. I. Joe, X. Chen, P. Ghaemi, K. Finkelstein, G. de La Peña, Y. Gan, J. Lee, S. Yuan, J. Geck, G. MacDougall, T. Chiang, S. Cooper, E. Fradkin, and P. Abbamonte, Nat. Phys. **10**, 421 (2014).

[71] The fact that the frequencies along the branch remain positive and the calculations do not predict the instability of the HT phase most likely highlights the shortcomings of the standard GGA functional employed within this study to properly resolve the very flat energy surface region separating the HT and LT phase of Sc_3CoC_4.

[72] C. B. Scruby, P. M. Williams, and G. S. Parry, Philos. Mag. **31**, 255 (1975).

[73] J. P. Pouget, C. R. Phys. **17**, 332 (2016).

[74] J. P. Pouget, R. Moret, A. Meerschaut, L. Guemas, and J. Rouxel, J. Phys. Colloq. **44**, C3-1729 (1983).

[75] K. Ishida and G. Honjo, J. Phys. Soc. Jpn. **34**, 1279 (1973).

[76] R. Xu and T. C. Chiang, Z. Kristallogr. Cryst. Mater. **220**, 1009 (2005).

[77] C. Milesi-Brault, C. Toulouse, E. Constable, H. Aramberri, V. Simonet, S. de Brion, H. Berger, L. Paolasini, A. Bosak, J. Íñiguez, and M. Guennou, Phys. Rev. Lett. **124**, 097603 (2020).

[78] B. Wehinger, Ph.D. thesis, Universite de Grenoble, 2014.

[79] E. Constable, S. Raymond, S. Petit, E. Ressouche, F. Bourdarot, J. Debray, M. Josse, O. Fabelo, H. Berger, S. deBrion, and V. Simonet, Phys. Rev. B **96**, 014413 (2017).

[80] R. B. Neder and T. Proffen, *Diffuse Scattering and Defect Structure Simulations*, 1st ed. (Oxford University Press, Oxford, 2008), Chap. 6.2, pp. 75–79.

[81] C. Giacovazzo, *Fundamentals of Crystallography*, 3rd ed., edited by C. Giacovazzo (Oxford University Press, Oxford, 2011), Chap. 4.5, pp. 251–254.

[82] Only the relative phase of the cobalt and scandium atom displacements is of interest for the final value of $F(\mathbf{h})$. Thus, the value of ϕ for either the cobalt or the scandium atom displacements may be chosen arbitrarily as 0 or π.

[83] A wave vector $\mathbf{q} = (0.5, 0.5, p)^T$ must be used in the calculation of the superstructure reflection intensity along arbitrary lines $[h, 1.5, p]$ parallel to $[h, 1.5, 0]$.

[84] In the present simplified structure containing only cobalt atoms, two cobalt atoms at the fractional coordinates $(0, 0.5, 0)$ and $(0.5, 0, 0.5)$ have to be taken into account in the calculation of $G_{Co}(\mathbf{h} \pm \mathbf{q})$.

[85] This is the situation found in the LT structure of Sc_3CoC_4 published earlier, see Ref. [30].

[86] Only the strongly displaced scandium atoms at the fractional coordinates $(0.5, 0, 0)$ and $(0, 0.5, 0.5)$ are taken into account.

[87] More precisely, a twofold rotation of the diffraction pattern about a^* has to be performed corresponding to a twofold rotation about a as twin law in real space.

[88] T. Proffen and R. B. Neder, J. Appl. Crystallogr. **30**, 171 (1997).